BOUNDARY-LAYER WATER VAPOR VARIATIONS OBSERVED BY RAMAN LIDAR AT THE ARM SGP SITE

Kyoko Taniguchi and Zhien Wang

Department of Atmospheric Science, University of Wyoming, Laramie, Wyoming 82071, USA,
E-mail: kyoko76@uwyo.edu, zwang@uwyo.edu

ABSTRACT

As a part of the Atmospheric Radiation Measurement (ARM) program, the Raman lidar has been in operation at the Southern Great Plane (SGP) site Cloud and Radiation Testbed (CART) facility in Northern Oklahoma for nearly 10 years. The long-term water vapor measurements from the Raman lidar provide a unique data set to understand tropospheric water vapor. In this study, Raman lidar data obtained over 5 years at the SGP site are used to examine the temporal or spatial variations of the boundary layer water vapor.

1. INTRODUCTION

Water vapor is one of the most important substances in the atmosphere due to its interactions with atmospheric processes, including acting as an effective greenhouse gas. However, its temporal and spatial inhomogeneity makes related effects heterogeneous and difficult to be estimated. To acquire better knowledge of water vapor distributions on different temporal and spatial scales, various measurement methods have been employed.

Since Melfi et al. [1] and Cooney [2] introduced the Raman lidar in the late 1960's, it has become a well-established method for water vapor observation [3]. In addition to its simple concept, the Raman lidar has some advantages over other instruments. GPS-based measurements derive the total water vapor from measured signal delays along the signal's paths. Thanks to its great accessibility, GPS archives fine enough temporal and spatial resolutions to capture some of the water vapor variation [4]. Although coarsely resolved vertical water vapor measurements are available at a few locations, the GPS data obtained is normally the total precipitable water vapor. The traditional two-channel microwave radiometer (MWR) can also only provide vertically integrated precipitable water vapor. Unlike GPS or MWR measurements, the Raman lidar provides vertically resolved water vapor observations. Also, the Raman lidar is capable of obtaining continuous measurements rather than point measurements. Although radiosondes provide valuable observations of water vapor and other atmospheric properties, the temporal or spatial resolution of such in situ measurements are too coarse for water vapor variation characterization. Hence, the Raman lidar supplies the best measurements for studying temporal and spatial variations of water vapor. Like any other instrument, the Raman lidar also has limitations. The day-time solar background is a serious problem for free troposphere water vapor measurements, because the Raman scattering intensity is weak and water vapor concentration decreases with height rapidly. To overcome this difficulty, several approaches have been demonstrated; noise subtraction [5], UV solar-blind wavelength [6], dual field of views [7], turn-key automated system [8], and narrow-field view and narrow-bandwidth filters [9]. Accordingly, the Raman lidar has the capability to monitor water vapor variation continuously over long periods with an uncertainty of 5% or less and detection limit of 0.002g/kg [10, 11].

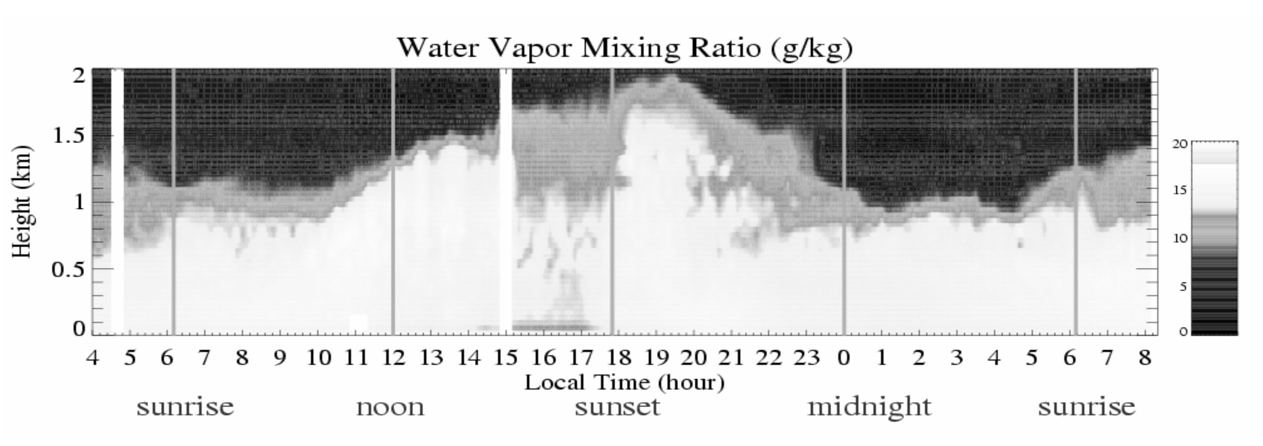

Figure 1. The water vapor mixing ratio as observed by Raman lidar at the SGP site on 25 September 1998. Narrow vertical lines indicate the calculated sunrise, noon, sunset, and midnight times.

2. INSTRUMENTS and DATA

The CART Raman lidar transmits a third harmonic Nd:YAG laser (355nm, 400 mJ energy/pulse) vertically with a repetition rate of 30Hz. The laser beam is expanded to 13cm in diameter for eye-safety. A 61-cm-diameter receiver collects Raman signals from nitrogen and water vapor at wavelengths centered at 387nm and 408nm, respectively, as well as elastic signals at 355nm. Since water vapor mixing ratio is the mass ratio of water vapor and dry air within a given volume, it can be derived from the Raman signals of water vapor and nitrogen. The ARM Raman lidar data is available as calibrated profiles of water vapor mixing ratio together with the associated random error estimation. The technical and data processing details of the Raman lidar system at the SGP site are discussed in [8,10,12]. Although the Raman lidar provides measurements over 0.060~3.5km and 0.060~8km for daytime and nighttime, respectively, the present study focuses on the lowest 2km of the atmospheric layer where most of the water vapor occurs. At the SGP site, tower measurements are available to fill in the lowest 60m blank of the Raman lidar measurement. The authors are aware that the tower data would provide valuable information, but only the Raman lidar data was used at this time.

The Raman lidar data analyzed in the present study was obtained between March 1998 and August 2003 almost continuously at the SGP site. Because of the calibration routine, as well as the mechanical and environmental conditions, the Raman lidar data quality is not uniform. To ensure the quality of the study, screening processes were applied to the whole dataset. First, data used for analysis must contain no more than 3.5 hours of break time within a day, and no more than 1-hour break within the calculation periods (Δt). Second, only data with estimated random error less than 15% are used for analysis, which minimizes the potential noise impact on the results. The days that satisfied the screening requirements were 218 days, 182 days, 191 days, and 127 days for spring (March, April, May), summer (June, July, August), fall (September, October, November) and winter (December, January, February), respectively. Unfortunately, the Raman lidar has problems under rainy, low-level cloud and foggy conditions [13]. Under such conditions, the observation may contain severe noise. Thus, data under rainy or foggy conditions were excluded in the present study. Although the presence of mid- and high-level clouds reduces the observation range to some degree, its effects are expected to be insignificant in the lowest 2km layer. Hence, the selected data still represents conditions under both clear and cloudy sky.

Table 1. The starting and ending time of mean and standard deviation calculations for each solar event.

Solar Event	Starting Time	Ending Time
Before Sunrise	$t_{rise1} - \Delta t$	t_{rise1}
After Sunrise	t_{rise1}	$t_{rise1} + \Delta t$
Noon	$t_{noon} - 0.5\Delta t$	$t_{noon} + 0.5\Delta t$
Sunset	$t_{set} - \Delta t$	t_{set}
Midnight	$t_{night} - 0.5\Delta t$	$t_{night} + 0.5\Delta t$

Note: Δt represents the length of the calculation period. It ranges between 10min and 4hrs.

For each day, sunrise, noon, sunset, and midnight times (these will be referred as solar events hereafter) were calculated based on the geographical coordinates of the SGP site and the time of the year. In the present study, noon (t_{noon}) and midnight (t_{night}) are referred to the mid-time between sunrise (t_{rise1}) and sunset (t_{set}), and between t_{set} and sunrise of next day (t_{rise2}) as shown in Fig.1. For convenience, a day in this study starts at sunrise time and ends at next sunrise, rather than UTC or local time. Multifilter rotating shadowband radiometer (MFRSF) data collected at the SGP site was used to verify the accuracy of the solar time calculations.

3. METHODOLOGY and RESULTS

The mean and standard deviation of water vapor mixing ratio over periods from 10 minutes to 4 hours were calculated 5 times a day, arranged around the solar events. The starting and ending times of the calculations are summarized in Table 1. The daily means and standard deviations were used to generate monthly and seasonal statistics. Because each month contains a different number of days that satisfied the screening processes, the seasonal averages were weighted by day rather than by month. All standard deviations were normalized by the corresponding means.

To examine the temporal variation of the water vapor mixing ratio, Fig.2 shows the normalized standard deviation as a function of the calculation period length (Δt), from 10 minutes to 4 hours. For each period Δt, the normalized standard deviation represents the standard deviations averaged over a 2km-layer. Regardless of the season or time of the day, the variation increases with the length of Δt. The winter variation shows an especially rapid growth as Δt increases. The summer variation is the least sensitive to changes in Δt. The largest seasonal differences are detected around sunrise, and the smallest around noon. Unlike the seasonal relative differences, the diurnal relative differences are reduced with increasing Δt.

Interestingly, the spring diurnal cycle shows a similar trend to the summer, and similarly the fall to winter.

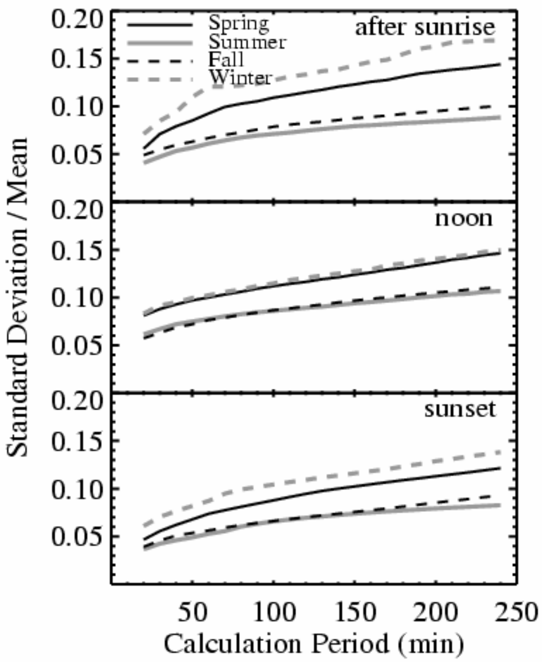

Figure 2. The average temporal variation of water vapor mixing ratio within the lowest 2km boundary layer as a function of Δt during after-sunrise, noon, and sunset.

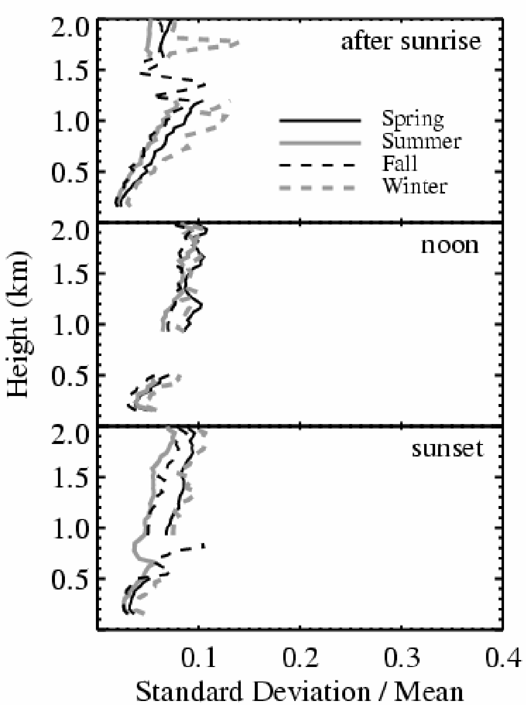

Figure 3. The vertical dependency of normalized standard deviations of water vapor mixing ratio over 1-hour periods for the four seasons during after-sunrise, noon, and sunset.

The plot of the mean water vapor mixing ratio as a function of height shows great seasonal differences. However, the strong temperature dependency of the water vapor saturation mixing ratio prevents better characterizations of the vertical variations of water vapor mixing ratio without continuous temperature profiles. Therefore, the vertical dependency of mean water vapor mixing ratio is not studied here. To study the vertical dependency of the water vapor mixing ratio variation, the normalized standard deviation as a function of height is illustrated in Fig.3. The winter profile indicates maximum relative variations, whereas the summer profile shows a minimum. Even at 150m height, the relative variation in winter is roughly 30% greater than that in summer. The most remarkable result of Fig.3 is the seasonal dependency of the vertical trends. The increasing rate is the largest in winter and the smallest in summer. These seasonal differences are more pronounced around noon for most altitudes. The seasonal and diurnal differences seem to be affected by the boundary layer mixing, but a detailed study has not been performed yet.

In Fig.3, the profiles show blanks at heights between 1.2km and 1.6km for the sunrise and midnight profiles, and between 0.6km and 0.9km for the noon profiles. In the CART Raman lidar, a dual field of view receiving system is employed to improve the observation range. However, the system introduces large error for the region around the transitional altitude. As a result, profiles have discontinuities due to high random error data, which was excluded in the screening process as discussed in section 2. Reference [8] discussed characteristics of the dual field of view system, and modifications to reduce the discrepancy between the dual field of view measurements. We will explore new approaches to optimally merge the dual view water vapor measurements to better characterize the vertical dependencies of water vapor variations.

4. SUMMARY

Raman lidar data was used in order to study water vapor horizontal inhomogeneity in the boundary layer. Over 5 years of data were acquired at the SGP-site CART facility as a part of the ARM program. To ensure reliable results, screening processes were applied to the data, which reduced the total data down to 718 days. Within the 2km layer of the lowest atmosphere, means and standard deviations over various periods (10min $\leq \Delta t \leq$ 4hr) were calculated 5 times a day based on the calculated solar event times. To assess the seasonal impacts on the water vapor variation, seasonal values were derived from daily results.

For temporal variations, 2km-average normalized standard deviations were plotted as a function of Δt.

Winter shows the largest variation, whereas summer indicates the least. Seasonal differences appear most around sunrise. However, the seasonal relative variations increase as Δt increases, whereas the diurnal relative variations decrease with increasing Δt. Similarities can be observed between spring and summer, as well as between fall and winter, especially around noon.

Also, the vertical dependency of temporal variations was seasonally analyzed. Although the profiles contain discontinuities due to the high random error at transitional altitudes of the dual field of view, the profiles provide an overview of the vertical dependency of the seasonal water vapor variation. In general, the variation increases with height, and the increasing rates are seasonally influenced. Rapid changes with height are observed in winter and gradual changes are observed in summer. Therefore, seasonal differences at solar events are enhanced at higher altitudes. The diurnal differences seem to have less influence than seasonal differences. The boundary layer mixing seems to have an important role in the seasonal and diurnal differences.

In the future, the relationship between the water vapor mixing ratio variation and boundary layer mixing will be analyzed in details. Also, the vertical water vapor mixing ratio variations will be performed with adequate temperature profiles. To better understand the water vapor variations, meteorological and other observations around the SGP site will be used for the analysis.

ACKNOWLEDGMENTS

Data were obtained from the Atmospheric Radiation Measurement (ARM) Program sponsored by the U.S. Department of Energy, Office of Science, Office of Biological and Environmental Research, Environmental Sciences Division.

REFERENCES

1. Melfi, S. H., J. D. Lowrence, and M. P. McCormick, 1969: Observation of the Raman scattering by water vapor in the atmosphere, *Appl. Phys. Letters*, **15**, 295-297.

2. Cooney, J. A., 1968: Measurements on the Raman component of laser atmospheric backscatter, *Appl. Phys. Letters*, **12**, 40-42.

3. Whiteman, D. N., S. H. Melfi, R. A. Ferrare, 1992: the Raman Lidar System for Measurement of Water Vapor and Aerosols in the Earth's Atmosphere, *Appl Opt.*, **31**, 3068-3082.

4. Bengtsson, L., et al., 2003: The use of GPS measurements for water vapor determination, *Ameri. Meteor. Soc.*, **84**, 1249-1258.

5. Hirschfeld, T., and E. R. Schildkraut, 1973: Remote spectroscopic analysis of ppm-level air pollutants by the Raman spectroscopy, *Appl. Phys. Lett.*, **22**, 38-40.

6. Renaut, D. and R. Capitini, 1988: Boundary-layer water vapor probing with a solar-blind the Raman lidar: validations, meteorological observations and prospects, *J. Atmos. Oceanic Technol.*, **5**, 585-601.

7. Bisson, S. E., J. E. M. Goldsmith, and M. G. Michell, 1999: Narrow-band, narrow-field-of-view the Raman lidar with combined day and night capability for tropospheric water-vapor profile measurements, *Appl. Opt.*, **38**, 1841-1849.

8. Goldsmith, J. E. M., F. H. Blair, S. E. Bisson, and D. D. Turner, 1998: Turn-key the Raman lidar for profiling atmospheric water vapor, clouds, and aerosols, *Appl. Opt.*, **37**, 4979-4989.

9. Whiteman, David N., 2003: Examination of the Traditional the Raman Lidar Technique. I. Evaluating the temperature-dependent lidar equations, *Applied Optics*, **42**, No. 15, 2571-2592.

10. Turner, D. D., R. A. Ferrare, L. A. Heilman, W. F. Feltz, and T. P. Tooman, 2002: Automated retrievals of water vapor and aerosol profiles from an operational the Raman lidar, *J. Atmos. Oceanic Technol.*, **19**, 37-50.

11. Whiteman, D. N., et al., 2006: Analysis of the Raman lidar and radiosonde measurements from the AWEX-G field campaign and its relation to Aqua validation. *J. Geophys. Res.*, (in press).

12. Turner, D. D. and J. E. M. Goldsmith, 1999: Twenty-four-hour the Raman lidar water vapor measurements during the Atmospheric Radiation Measurement Program’s 1996 and 1997 water vapor intensive observation periods, *J. Atmos. Oceanic Technol.*, **16**, 1062-1076.

13. Wechwerth, T.M., V. Wulfmeyer, R.M. Wakimoto, R.M. Hardesty, J.W. Wilson, and R.M. Banta, 1999: NCAR-NOAA Lower-Tropospheric Water Vapor Workshop, *Bull. Amer. Meteor. Soc.*, **80**, 2339-2357.